# Modeling of electron-electron scattering in Monte Carlo simulation of quantum cascade lasers

Olivier Bonno, Jean-Luc Thobel, François Dessenne

# Modeling of electron–electron scattering in Monte Carlo simulation of quantum cascade lasers

Cite as: J. Appl. Phys. **97**, 043702 (2005); https://doi.org/10.1063/1.1840100
Submitted: 12 July 2004 • Accepted: 02 November 2004 • Published Online: 21 January 2005

**Olivier Bonno, Jean-Luc Thobel and François Dessenne**

JOURNAL OF APPLIED PHYSICS **97**, 043702 (2005)

# Modeling of electron–electron scattering in Monte Carlo simulation of quantum cascade lasers

Olivier Bonno,[a] Jean-Luc Thobel, and François Dessenne
*Institut d'Électronique, de Microélectronique et de Nanotechnologie, Département Hyperfréquences et Semiconducteurs, Unité Mixte de Recherche Centre National de la Recherche Scientifique (UMR CNRS) 8520, Université des Sciences et Technologies de Lille, Avenue Poincaré, BP 69, 59652 Villeneuve d'Ascq Cédex, France*

(Received 12 July 2004; accepted 2 November 2004; published online 21 January 2005)

A theoretical model of electron–electron scattering in multisubband systems is proposed and used to set up a Monte Carlo simulator of quantum cascade lasers. Special features of the electron–electron scattering model are the following: (i) A fast and accurate computation of bare potential matrix elements by means of Fourier analysis is developed. (ii) A screening model is proposed that allows us to describe intersubband matrix elements. (iii) Nonequilibrium screening factors, defined through an effective subband temperature for each subband, are periodically reevaluated. (iv) The developed algorithm makes use of rejection procedures in order to determine the correct number of scattering events as well as the distribution of the final states. Other characteristics of the model are the following: the energy levels and the wave functions are determined in a self-consistent way, the Pauli exclusion principle is included, and the periodicity of the structure is accounted for. This model is applied to the study of a terahertz resonant phonon quantum cascade laser. A large influence of the screening model on the subband population is demonstrated. For the considered design, emission at a frequency as low as 1 THz is confirmed. We have found that the magnitude of population inversion phenomena may be strongly sensitive to electron–electron scattering, reducing the possible performance near 1 THz. © *2005 American Institute of Physics*.
[DOI: 10.1063/1.1840100]

## I. INTRODUCTION

Over the past several years, quantum cascade lasers[1] (QCL's) have proved to be one of the best avenues for developing compact, low consumption solid-state sources in the midinfrared spectral region.[2] There is currently a tremendous effort[3,4] to extend their operating frequency range toward the terahertz region, where they have very few competitors, despite a wealth of attractive applications in, e.g., biomedical imaging, gas sensing, or molecular spectroscopy. At least two different designs of QCL's have experimentally demonstrated a terahertz emission. The first one, based on "chirped superlattice," has been proposed by Köhler *et al.*[3] In this QCL, extraction from the lower radiative state takes place via intraminiband transport and scattering. A different design, in which depopulation occurs by resonant polar optic-phonon scattering has been proposed by Williams *et al.*[5] For this kind of device, an operation at $\lambda \simeq 100\ \mu$m ($\sim$3 THz) up to a temperature of 77 K in pulsed mode has been recently reported.[6]

QCL's are unipolar semiconductor lasers based on transitions between subbands in a multi-quantum-well structure. Therefore, the lasing frequency can be varied in a wide range through a careful design of epitaxial structure. However, the complexity of QCL's makes highly desirable simulation tools that can deal with the complicated physical phenomena involved.

One of the most powerful tools for investigating charge transport in semiconductors is the Monte Carlo method. This technique has been extensively described in the literature.[7] Adapting Monte Carlo simulation to QCL is not a trivial task. First of all, since electrons move in the perpendicular direction, one has to treat a quantum transport problem. However, it has been shown that a Boltzmann-like formalism, disregarding phase coherent phenomena, is sufficient, at least for the stationary state.[8] With such an approach, the major problem arises from the huge number of possible scattering paths. This question is especially severe for terahertz QCL due to the large number of states involved in transport. Moreover, subbands are close in energy, separated by typically less than one phonon ($\hbar\omega_{po} \simeq 36$ meV in GaAs), and therefore they are strongly coupled by Coulomb scattering which can play a prominent role.

The modeling of this scattering mechanism in Monte Carlo simulation faces many difficulties of both technical and theoretical nature. For example, scattering rates depend on the distribution function, which is an unknown of the simulation, and thus has to be treated in a self-consistent way, generally using a rejection technique. Electron–electron scattering has been described in a number of papers,[9–13] but only for quantum wells with one or a few populated subbands. In QCL's, the situation is much more complex owing to the large number of levels, and thus form-factor evaluation requires a prohibitive computational cost. The need to account for screening in a many-subband (MS) system makes the situation even worse. However, this question has been rigorously addressed only for rather simple systems,[14] whereas for complex structures like QCL's, crude approxi-

[a]Electronic mail: olivier.bonno@laposte.net

 

mations are generally used. Therefore, a simplified MS model is needed, which throws a bridge between the simple but inaccurate single-subband screening model[15] (S3M) and the rigorous but time-consuming full MS model.

To this aim, we describe a Monte Carlo simulator, including electron–electron scattering, to study MS systems. Although we focus on the specific case of QCL, the model is quite general and can also be applied to study carrier–carrier scattering in any multi-quantum-well structure. A strategy to reduce drastically the computational cost of evaluating the form factor is developed. Some approximations are proposed in order to account for MS screening in a tractable way. Simple expressions for the screening parameters are derived using an effective subband temperature. They are reevaluated periodically during the simulation in order to account for the nonequilibrium conditions. As a test-bed example of a MS system, we apply our model to the structure proposed by Williams *et al.*[5] which, according to Lee and Wacker,[16] can also operate near 1 THz.

The remainder of this article is organized as follows. In Sec. II we describe the Monte Carlo model emphasizing the electron–electron scattering implementation and the screening model. The main results are presented in Sec. III. Finally, the main conclusions are summarized in Sec. IV.

## II. TRANSPORT MODEL

### A. General features: Electronic states

The determination of quantized energies as well as wave functions in heterostructures have been extensively described in a previous report[17] and will only be briefly outlined here. Electron states are determined by solving the coupled Schrödinger and Poisson equations. In the framework of the envelope function theory for a two-dimensional electron gas, the wave function $\phi_\nu(z)$ of the $\nu$th state is a solution of a Schrödinger-like equation,

$$\mathcal{H}\phi_\nu(z) = \varepsilon_\nu(\mathbf{K})\phi_\nu(z), \tag{1}$$

where $\mathcal{H}$ is the BenDaniel–Duke Hamiltonian,[18] $\mathbf{K}$ is the two-dimensional in-plane wave vector, $z$ is the coordinate along the confinement direction, and $\varepsilon_\nu(\mathbf{K})$ is the dispersion relation. Owing to nonparabolicity, $\mathcal{H}$ is itself dependent on energy, a fact that is accounted for following the method of Thobel *et al.*[19]

In theoretical studies,[20] one considers a QCL as an infinite repetition of an elementary sequence called a "stage." Thanks to this periodicity, wave functions and energy levels are determined using the following scheme: (i) the Schrödinger equation is solved on $2p+1$ stages; (ii) each wave function is assigned to a stage, according to the probability of presence. Then the states belonging to the central stage are replicated $2p$ times with proper shifts in space and energy; (iii) the potential is obtained from Poisson's equation, assuming conservation of electronic charge in each stage, so that one can define a local Fermi level. The calculation is iterated until self-consistency is achieved.

Recently, it has been shown that coherent phenomena in QCL's can be disregarded as long as short-time behavior is not under study.[8] Therefore, it is possible to neglect off-diagonal elements of the density operator, and to derive a Boltzmann-like equation for the diagonal components. Hence, perpendicular transport in QCL may be studied by means of a Monte Carlo simulation. Such a simulator is presented in this work, whose essential features are described in the following. The main scattering mechanisms are included, i.e., phonon (polar optic and acoustic, considering only bulk modes), ionized impurity, and alloy scattering.[17,19] These scattering rates are evaluated as a function of the in-plane wave vector accounting for nonparabolicity. In this work, only electron–electron scattering is treated in the parabolic approximation, which is widely used in the literature. This assumption, although very convenient, is not too severe for GaAs/AlGaAs systems, owing to the small conduction-band nonparabolicity coefficient. The coupling between adjacent stages is taken into account by evaluating all intra- and interstage matrix elements. In the Monte Carlo simulation, we account for the periodicity of the structures in the following way: an electron which undergoes an interstage transition is reinjected into the corresponding subband of the central stage.[20] Finally, degeneracy is included in the model following the approach described in Ref. 21.

### B. Electron–electron scattering

In this work, we only investigate the short-range part of the Coulomb interaction,[22] neglecting electron–plasmon scattering. We consider a "principal" electron in subband $\nu$ with two-dimensional wave vector $\mathbf{K}$ and a "partner" electron in subband $\mu$ with wave vector $\mathbf{P}$. The final states of these two electrons are, respectively, $|\nu'\mathbf{K}'\rangle$ and $|\mu'\mathbf{P}'\rangle$. Starting from the Fermi golden rule, the probability per unit time that the principal electron undergoes a Coulomb scattering is given by[23]

$$\lambda_{\nu\nu'}(\mathbf{K}) = \frac{m_e^*}{4\hbar^3\pi\mathcal{A}} \sum_{\mu,\mu',\mathbf{P}} f_\mu(\mathbf{P}) \int_0^{2\pi} d\theta |M_{\nu\mu\nu'\mu'}(Q)|^2, \tag{2}$$

where $m_e^*$ is the electron effective mass, $\mathcal{A}$ is the normalization area, $\mathbf{Q}=\mathbf{K}-\mathbf{K}'$ is the exchanged wave vector, $\theta$ is the angle between $\mathbf{P}-\mathbf{K}$ and $\mathbf{P}'-\mathbf{K}'$, and $M_{\nu\mu\nu'\mu'}(Q)$ is the matrix element of the transition.

The presence in Eq. (2) of the partner distribution function $f_\mu(\mathbf{P})$, which is unknown *a priori*, is a well-recognized difficulty[7] that is generally circumvented through a rejection technique.[10] This approach requires an upper bound of $\lambda_{\nu\nu'}(\mathbf{K})$ that we choose as

$$\Lambda_{\nu\nu'} = \frac{m_e^*}{2\hbar^3} \sum_{\mu,\mu'} n_\mu \mathcal{M}^2_{\nu\mu\nu'\mu'}, \tag{3}$$

where $n_\mu$ is the electronic density of subband $\mu$, and $\mathcal{M}^2_{\nu\mu\nu'\mu'}$ is the maximum of $|M_{\nu\mu\nu'\mu'}(Q)|^2$. During the simulation, scattering events are selected with the probabilities[24] $\Lambda_{\nu\nu'}$, but the rejection technique allows us to obtain the correct number of scattering events and the distribution of final states. In the simulation, when a simulated electron undergoes a Coulomb interaction, the partner electron is chosen at random from the ensemble, and its final subband $\mu'$ is selected according to the relative contribution $\mathcal{M}^2_{\nu\mu\nu'\mu'}$ in the

summation in Eq. (3). The Pauli exclusion principle is then applied to both the partner and principal electrons.[21] We account for exchange scattering between spin- $1/2$ particles with the symmetrized expression of the transition matrix element,[23]

$$|M_{\nu\mu\nu'\mu'}(Q)|^2 = \tfrac{1}{2}[|V_{\nu\mu\nu'\mu'}(Q)|^2 + |V_{\nu\mu\mu'\nu'}(Q')|^2 - V_{\nu\mu\nu'\mu'}(Q)V_{\nu\mu\mu'\nu'}(Q')], \quad (4)$$

where $\mathbf{Q}'=\mathbf{K}-\mathbf{P}'$, and $V_{\nu\mu\nu'\mu'}(Q)$ is the matrix element of the Coulomb potential.

The first step of electron–electron scattering rate computation is the determination of the bare potential matrix elements, which are expressed as

$$V^{\text{bare}}_{\nu\mu\nu'\mu'}(Q) = \frac{e_0^2}{2\kappa}\frac{F_{\nu\mu\nu'\mu'}(Q)}{Q}, \quad (5)$$

where $e_0$ is the elementary electronic charge, and $\kappa$ is the static permittivity assumed to be uniform all throughout the structure. Form factors are given by[10]

$$F_{\nu\mu\nu'\mu'}(Q) = \int\int \varphi_{\nu\nu'}(z_1)e^{-Q|z_1-z_2|}\varphi_{\mu\mu'}(z_2)dz_1dz_2, \quad (6)$$

where $\varphi_{\nu\nu'}(z)=\phi_\nu(z)\phi^*_{\nu'}(z)$. In Eq. (6), each integral extends over the whole length $L$ of the $2p+1$ stages, and a brute force computation of each coefficient is quite lengthy. One has to consider, for each value of $Q$, a number of coefficients proportional to the fourth power of the number of subbands $N_{\text{sb}}$ and, therefore, the direct use of Eq. (6) is definitely prohibitive for MS systems such as QCL. Previous investigations have made use of analytical expressions obtained assuming sine wave functions.[25] Obviously, such an assumption is no longer relevant here. However, it is always possible, without loss of accuracy, to use Fourier decomposition. As we will show, this leads to expressions which can be evaluated efficiently. It is convenient to work on $\varphi_{\nu\nu'}(z)$,

$$\varphi_{\nu\nu'}(z) \simeq \sum_{\sigma=-N_H}^{N_H} \gamma_\sigma^{\nu\nu'} \exp(i\sigma k_0 z), \quad (7)$$

where $i^2=-1$, $N_H$ is the number of retained harmonics, $\gamma_\sigma^{\nu\nu'}$ is the $\sigma$th Fourier coefficient, and $k_0=2\pi/L$.[26]

Rewriting Eq. (6) using the Fourier series of $\varphi_{\nu\nu'}(z_1)$ and $\varphi_{\mu\mu'}(z_2)$, one has to evaluate the following expression:

$$F_{\nu\mu\nu'\mu'}(Q) \simeq \sum_{\sigma_1=-N_H}^{N_H}\sum_{\sigma_2=-N_H}^{N_H} \gamma_{\sigma_1}^{\nu\nu'}\gamma_{\sigma_2}^{\mu\mu'}\mathcal{G}_{\sigma_1\sigma_2}(Q), \quad (8)$$

where

$$\mathcal{G}_{\sigma_1\sigma_2}(Q) = \int_0^L\int_0^L e^{i\sigma_1 k_0 z_1}e^{i\sigma_2 k_0 z_2}e^{-Q|z_1-z_2|}dz_1dz_2. \quad (9)$$

After some algebra, one finds

$$\mathcal{G}_{\sigma_1\sigma_2}(Q) = \frac{2LQ\delta_{\sigma_1,-\sigma_2}}{Q^2+\sigma_2^2k_0^2} + \frac{2(e^{-QL}-1)(Q^2+\sigma_1\sigma_2k_0^2)}{(Q^2+\sigma_1^2k_0^2)(Q^2+\sigma_2^2k_0^2)}, \quad (10)$$

where $\delta$ is the Kronecker function. Using Eq. (10) , it is easy to show that the double summation in Eq. (8) can be calculated by performing five summations over a single index, thus allowing to dramatically speed up the computation. For example, applying directly formula (6) with a typical length of 300 nm discretized into $N_z=3000$ points, each value of $F_{\nu\mu\nu'\mu'}(Q)$ requires $N_z^2\simeq 10^7$ operations. With our method and $N_H\simeq 100$, only $5\times 200=10^3$ operations are needed, hence saving CPU time in a ratio of $1:10^4$. Thus our method makes possible calculations which otherwise would have been out of reach.[27]

### C. Screening model

Dealing with two-dimensional screening phenomena in MS systems, such as QCL's, is a formidable task, requiring huge computational resources for evaluating the dielectric matrix. For this reason, screening is treated in an approximate manner. One generally assumes that only the lowest subband contributes to the screening. Therefore, there is a need for a tractable model which accounts for screening by several populated subbands and properly describes both intra- and intersubband scattering processes.

We adopt a static formulation of screening in the random-phase approximation. In this framework, screened potential matrix elements $V^{\text{scr}}_{\nu\mu\nu'\mu'}(Q)$ are solutions of the tensorial equation,

$$V^{\text{scr}}_{\nu\mu\nu'\mu'}(Q) = V^{\text{bare}}_{\nu\mu\nu'\mu'}(Q) + \sum_{\xi\xi'} V^{\text{bare}}_{\nu\xi\nu'\xi'}(Q)\Pi_{\xi\xi'}(Q)V^{\text{scr}}_{\xi\mu\xi'\mu'}(Q), \quad (11)$$

where $\Pi(Q)$ is the polarizability tensor.[28] The so-called single-subband screening model assumes that all electrons are in the ground subband, labeled by $g$ in the following. More precisely, the dielectric tensor reduces to a scalar dielectric function, and all screened matrix elements are given by

$$V^{\text{scr}}_{\nu\mu\nu'\mu'}(Q) \simeq \frac{V^{\text{bare}}_{\nu\mu\nu'\mu'}(Q)}{\kappa_g(Q)}, \quad (12)$$

where $\kappa_g(Q)=1-V^{\text{bare}}_{gggg}(Q)\Pi_{gg}(Q)$. However, it has been shown by Lee and Galbraith,[14] that the use of a single-subband dielectric function $\kappa_g(Q)$ for modeling intersubband transitions leads to erroneous screened potential matrix elements. These authors argued that in MS systems, one should account for intersubband polarizability $\Pi_{\xi\xi'}$, $\xi\neq\xi'$, and unscreened potential matrix elements. In other words, one has to solve the full $N_{\text{sb}}^4\times N_{\text{sb}}^4$ equation system [Eq. (11) ]. In the literature, this has only been achieved for rather simple systems, e.g., for an infinite quantum well.[29] In QCL's, a complete resolution is numerically intractable owing to the large number of levels, thus some approximations must be adopted. In this work, we propose to only retain in Eq. (11) the couples $(\xi,\xi')=(\nu,\nu')$, $(\nu',\nu)$ and $(g,g)$, in order to ob-

tain a system which is explicitly solved, giving

$$V^{\mathrm{scr}}_{\upsilon\mu\upsilon'\mu'}(Q) = \frac{D_g(Q)}{D_{\nu\nu'g}(Q)}\left[ V^{\mathrm{bare}}_{\upsilon\mu\upsilon'\mu'}(Q) + \frac{N_{\nu\nu'g}(Q) V^{\mathrm{bare}}_{g\mu g\mu'}(Q)}{D_g(Q)} \right], \tag{13a}$$

with

$$D_g(Q) = 1 - V^{\mathrm{bare}}_{gggg}(Q)\Pi_{gg}(Q), \tag{13b}$$

$$N_{\nu\nu'g}(Q) = V^{\mathrm{bare}}_{\upsilon g\upsilon' g}(Q)\Pi_{gg}(Q), \tag{13c}$$

$$D_{\nu\nu'g}(Q) = D_g(Q) \times [1 - V^{\mathrm{bare}}_{\nu\nu\nu'\nu'}(Q)\Pi_{\nu\nu'}(Q)] - N_{\upsilon\upsilon' g}(Q) V^{\mathrm{bare}}_{g\upsilon g\upsilon'}(Q)\Pi_{\upsilon\upsilon'}(Q). \tag{13d}$$

The above formulas have been derived considering that only subband $g$ contributes to the screening. They can be generalized to the case where several significantly populated subbands, labeled $\{g_1, g_2, \ldots\}$, are effective in the screening. In that case, we replace, in Eqs. (13a)–(13d), each term containing $\Pi_{gg}$ by the corresponding summation over $g_j$. For example, in Eq. (13b), one has to replace

$$V^{\mathrm{bare}}_{gggg}(Q)\Pi_{gg}(Q) \rightarrow \sum_j V^{\mathrm{bare}}_{g_j g_j g_j g_j}(Q)\Pi_{g_j g_j}(Q). \tag{14}$$

### D. Nonequilibrium electron–electron scattering

Since, in QCL, subband populations evolve in nonequilibrium conditions, it is necessary to reevaluate the summation in (3) during the simulation. Moreover, the distribution function enters the definition of the polarizability matrix elements, and thus electron occupancies also influence electron–electron probabilities through $\mathcal{M}^2_{\nu\mu\nu'\mu'}$. In this subsection we propose a method in order to account for the nonequilibrium screening in a self-consistent way.

In the static long-wavelength limit, diagonal elements of the polarizability tensor take the following expression[14]

$$S_\nu \equiv \Pi_{\nu\nu}(Q \rightarrow 0) = -\rho_\nu f_\nu(0), \tag{15a}$$

where $\rho_\nu = m^*_\nu/(\pi\hbar^2)$ is the density of states, and $m^*_\nu$ is the effective mass of subband $\nu$. Nondiagonal elements are given by

$$\Pi_{\nu\mu}(Q \rightarrow 0) = \frac{n_\nu - n_\mu}{\varepsilon_\nu - \varepsilon_\mu}, \tag{15b}$$

where $\varepsilon_\nu$ is the eigenenergy associated with the $\nu$th state.[30] In most papers,[23,31,32] $S_\nu$ is recalculated during the simulation using Eq. (15a) with the current value of $f_\nu(0)$. However, in practice this value depends critically on the discretization of the phase space and, moreover, it strongly fluctuates. Thus, it is more convenient to use global parameters,[33] such as subband density and electron temperature, which are less noisy than the value of $f_\nu(\mathbf{K})$ at a single point. To this aim, we use expressions obtained for a Fermi–Dirac distribution and we assume that they remain acceptable in QCL, provided that an effective temperature $T_\nu$ is properly evaluated. In this scheme, Eq. (15a) becomes $S_\nu = -\rho_\nu f_\nu(0) = -\rho_\nu\{1 - \exp[-n_\nu/(\rho_\nu k_B T_\nu)]\}$, where $k_B$ is the Boltzmann constant. We choose to define the electron temperature $T_\nu$ through a parameter, denoted here as $\Gamma_\nu$, which can be interpreted as a measure of the broadening of the energy distribution,

$$\Gamma_\nu = \int_0^\infty f_\nu(\varepsilon)[1 - f_\nu(\varepsilon)]d\varepsilon = k_B T_\nu \left[ 1 - \exp\left( -\frac{n_\nu}{\rho_\nu k_B T_\nu} \right) \right], \tag{16}$$

where $f_\nu$ is normalized so as to recover the subband density,

$$\int_0^\infty \rho_\nu f_\nu(\varepsilon)d\varepsilon = n_\nu. \tag{17}$$

Equation (16) is valid for a Fermi–Dirac distribution in a parabolic band and for a spherically symmetric distribution function, however, it can be generalized to the nonparabolic case. For a nondegenerate gas, $\Gamma_\nu$ is given by

$$\Gamma_\nu \simeq \frac{n_\nu}{\rho_\nu}\left( 1 - \frac{n_\nu}{2\rho_\nu k_B T_\nu} \right). \tag{18}$$

Equation (15a) becomes

$$S_\nu \simeq -\frac{n_\nu}{k_B T_\nu} \simeq -\frac{2\rho_\nu}{n_\nu}(n_\nu - \rho_\nu \Gamma_\nu). \tag{19}$$

In the general case Eq. (16) is solved iteratively to give $T_\nu$. We have verified that the use of the lattice temperature instead of $T_\nu$ would strongly overestimate the effect of screening, and hence underestimate electron–electron scattering. The polarizability tensor and all electron–electron scattering rates are updated at regularly spaced times, or whenever the subband population changes significantly.

## III. RESULTS

In this section, we present some results of Monte Carlo simulation of resonant phonon QCL. In this kind of device, the lower laser state is separated from the so-called "injector states" by one phonon energy, so that polar optic-phonon scattering provides a very efficient depopulation mechanism. Moreover, the injector consists only of a few wells leading to much simpler structures than chirped superlattice QCL. For example, a published[5] structure of this kind is composed of four wells per stage, and has demonstrated lasing operation at 3.4 THz up to 65 K. Its main drawback is the high threshold current probably due to parasitic current paths.[34] Recently, Lee and Wacker[16] suggested that this structure can also operate at lower frequencies, close to 1 THz. The corresponding transitions occur between levels assigned to different periods of the structure. Therefore, for an unambiguous description, one must take as the stage two elementary periods of the initial structure. Within this picture, all lasing transitions occur between states assigned to the same stage. Following this point of view, in the remainder of this section, we consider that a stage consists of eight wells.

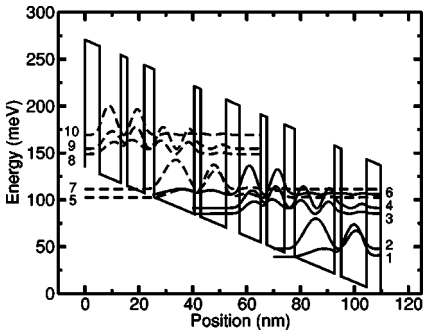


FIG. 1. Calculated potential profile and squared wave functions of the $GaAs/Al_{0.15}Ga_{0.85}As$ QCL (Ref. 5). The Schrödinger and Poisson equations have been solved over $2p+1=3$ stages. For readability, only the central stage is shown here. The lattice temperature is 44 K, the external applied field is 12.2 kV $cm^{-1}$, and the sheet density is $5.6\times10^{14}$ $m^{-2}$. The energy separation between levels 2 and 3, as well as between states 7 and 8, matches the polar optic-phonon energy.

Figure 1 shows the band profile and squared wave functions of this structure under an external field $F=12.2$ kV $cm^{-1}$, at a lattice temperature $T_{\text{latt}}=44$ K, and for a sheet density $N_s=5.6\times10^{14}$ $m^{-2}$ per stage. Radiative transitions experimentally reported by Williams *et al.* are $6\rightarrow4$ and $10\rightarrow9$. Those theoretically investigated by Lee *et al.* near 3 and 1 THz are $5\rightarrow4$ and $7\rightarrow6$, respectively. In the following discussion, we denote the former by "Class A" transitions, and the latter by "Class B" transitions. Table I summarizes the calculated energy separations and the dipole matrix elements for both Class A and B.

The first point we wish to discuss is the influence of the screening model for intra- and intersubband potential matrix elements. For the calculation of bare potential matrix elements, we take $N_H=100$, which is sufficient to satisfy the Parseval relation with an accuracy of up to $10^{-5}$. Three screening models are considered: (i) our screening model, (ii) the single-subband screening model, and (iii) the complete inversion of the dielectric matrix, i.e., solving Eq. (11). For cases (i) and (ii), we assume that only the first subband contributes to the screening, so that $g=1$ in Eqs. (12) and (13a)–(13d).

First, we examine the case of a purely intrasubband transition. As an illustration, Fig. 2 presents $V_{2222}$ for the three considered screening models. They all yield approximately the same results, and prevent the divergence of the bare potential matrix element in the long-wavelength limit.

We now turn our attention to intersubband transitions illustrated by Fig. 3. The considered example $V_{5665}$ is representative of "intersubband interactions resulting in an intersubband transition," according to the terminology of Lee *et al.*[14] One can see that a single-subband screening model leads to an incorrect behavior of the screened matrix element for small values of $Q$, as pointed out by Lee and Galbraith.[14] One notices, in particular, that $V_{5665}(Q)$ vanishes at $Q=0$, resulting in a significant suppression of the interaction. This model has two consequences on electron–electron scattering: (i) an underestimation of scattering rates by more than a factor of $10^3$ in the considered case ($5\rightarrow6$ and $6\rightarrow5$) and (ii) an erroneous determination of final states at the end of the rejection procedure. With our model, the screened potential is fairly close to the one obtained by inversion of the dielectric matrix and exhibits the expected behavior for $Q\rightarrow0$.

TABLE I. Calculated energy separations $\Delta\varepsilon_{\nu\mu}$ and dipole matrix elements $z_{\nu\mu}$ for the transitions of interest.

| Transition $\nu\rightarrow\mu$ | $\Delta\varepsilon_{\nu\mu}$(meV) | $z_{\nu\mu}$(nm) |
|---|---|---|
| Class A | | |
| $6\rightarrow4$ | 14.8 | 5 |
| $10\rightarrow9$ | 14.8 | 5 |
| Class B | | |
| $5\rightarrow4$ | 11.4 | 3.8 |
| $7\rightarrow6$ | 5.5 | 6.4 |

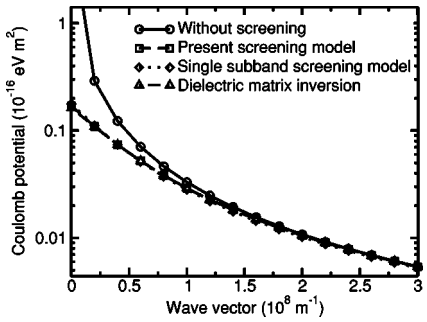


FIG. 2. The matrix element $V_{2222}$ for different screening models as a function of the wave vector $Q$ at the beginning of the simulation. Equations (12) and (13a)–(13d) are applied with $g=1$. Solid line: without screening, dashed line: our screening model, dotted line: a single-subband screening model, dashed-dotted line: inversion of the dielectric matrix considering the ten subbands of Fig. 1. These three last curves are almost indistinguishable.

We now present the results of the Monte Carlo simulation of the structure of Fig. 1. Simulation parameters are the conduction-band discontinuity $\Delta E_c$ between GaAs and AlGaAs estimated using a 62:38 rule, the number of subbands $N_{\text{sb}}=60$, and the electron effective masses of $m_e^*=0.067$ in the well and $m_e^*=0.08$ in the barrier. We monitor 4000 electrons during 200 ps using a constant time step $\Delta t=2$ fs.

To discuss the influence of the screening model, we show in Fig. 4 the distribution of electron density among the different subbands for the different screening models. The

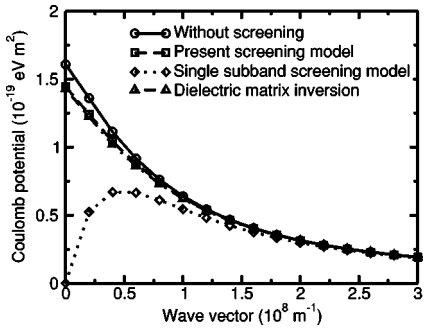


FIG. 3. The matrix element $V_{5665}$ for different screening models as a function of the wave vector $Q$ at the beginning of the simulation. Equations (12) and (13a)–(13d) are applied with the same parameters as in Fig. 2. Solid line: without screening, dashed line: our screening model, dotted line: a single-subband screening model, dashed-dotted line: inversion of the dielectric matrix.

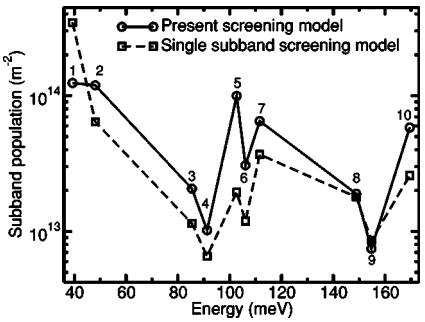


FIG. 4. The occupancy of the different subbands for two screening models. Only discrete values, shown by the symbols, are meaningful, however, for readability these symbols have been connected by lines. Circles: our screening model, squares: single-subband screening model.

S3M, frequently used in the literature, e.g., in Ref. 15, is compared to our model with the polarizability calculated as described in Sec. II D. For the latter case, we assume that the four most populated subbands contribute to the screening. Hence, in the steady state, subbands 1, 2, 5, and 7 have been used. In the following discussion, these parameters are assumed each time we refer to our screening model. We observe that the choice of the screening model affects strongly the populations. Compared to S3M, the use of our model decreases the population of level 1 from $3.5\times10^{14}$ to $1.2\times10^{14}$ m$^{-2}$, and consequently the occupancy of other states increases. As a result of this population redistribution, the magnitudes of the population inversion phenomena are significantly altered. For example, with our model the amplitude of population inversion $n_5-n_4$ is about $9\times10^{13}$ m$^{-2}$, ten times greater than with S3M.

To better understand the influence of electron–electron scattering, we investigate in Fig. 5 the population of the different subbands with and without carrier–carrier interaction. One can see that intercarrier scattering strongly influences the population repartition between the subbands, and leads to contrasting behaviors concerning population inversions. Indeed, Class A population inversion phenomena are clearly enhanced by electron–electron scattering, e.g., the amplitude of population inversion of the $10\rightarrow9$ transition is about $5\times10^{13}$ m$^{-2}$, five times greater than when carrier–carrier interaction is not accounted for. Moreover, this value of population inversion shows a reasonably good agreement with other published results.[5,34] On the contrary, carrier–carrier scattering seems to reduce the possible performance around

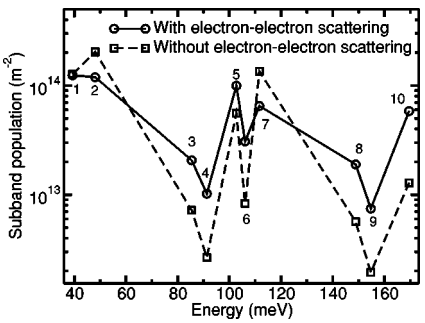


FIG. 5. The subband occupancy with and without carrier–carrier scattering. As in Fig. 4, the symbols represent the different eigenenergies. Circles: with electron–electron scattering using our screening model, squares: without electron–electron scattering.

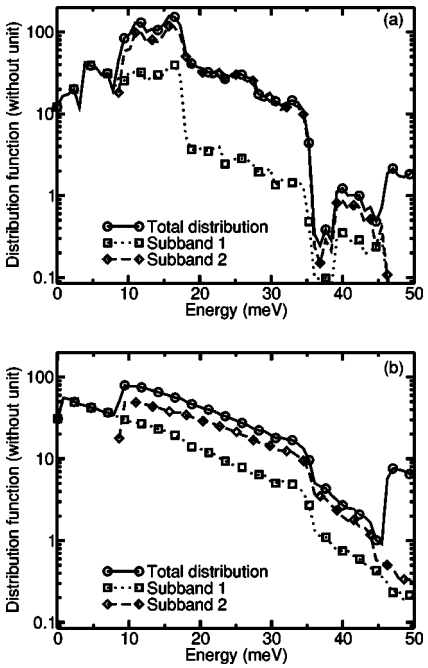


FIG. 6. Distribution function as a function of the energy. The energy reference of all the curves is the bottom of the first subband: (a) without electron–electron scattering and (b) with electron–electron scattering. Solid line: the total distribution function, dotted line: distribution function of subband 1, dashed line: distribution function of subband 2.

1 THz, the population inversion of the Class B transition $7\rightarrow6$ is about four times smaller with carrier–carrier scattering than without it. Let us now explain this result on the basis of scattering lifetimes $\tau^{\mathrm{int}}_{\nu\rightarrow\mu}$ calculated from the simulation, where int labels the interaction mechanism, polar optic (po) or electron–electron (ee). We find $\tau^{\mathrm{ee}}_{7\rightarrow6}=5.6$ ps, $\tau^{\mathrm{po}}_{7\rightarrow6}=53$ ps, and a total lifetime $\tau_7\sim1.2$ ps. The depopulation of subband 7 is mainly due to direct electron–electron $7\rightarrow6$ transitions. This leads to the repopulation of subband 6 and to a decrease of the population of subband 7 by almost a factor 2. Thus, the $7\rightarrow6$ population inversion, strongly affected by electron–electron scattering, is only $n_7-n_6\sim3\times10^{13}$ m$^{-2}$.

To further investigate the influence of this scattering mechanism, we present in Fig. 6 the distribution function as a function of the energy, with and without electron–electron interaction. When carrier–carrier scattering is not included [Fig. 6(a)], one can observe that the distribution function presents a quite complex structure, with a number of peaks presumably related to various thresholds of inelastic transitions. As seen in Fig. 6(b), with electron–electron scattering, the distribution function exhibits a smoother shape and, in particular, the dip for energies slightly above 36 meV ($\sim\hbar\omega_{\mathrm{po}}$) disappears in the presence of intercarrier interaction. Indeed, electron–electron scattering redistributes the energy in the electron gas, owing to the many degrees of freedom in the conservation laws. As reported by many authors,[7,10] carrier–carrier scattering tends to set up a heated Maxwellian distribution with a given electron temperature $T_\nu$.

We now focus on the calculated electron temperatures $T_\nu$ reported in Table II. These values have been obtained at the end of the simulation following the method described in Sec.

TABLE II. Calculated electron subband temperatures for the QCL of Fig. 1 with and without electron–electron (ee) scattering. Note that, when ee scattering is not included, the determination of temperature is difficult for subbands 3 and 8, because their population is very low (see Fig. 5). The lattice temperature is 44 K.

| $\nu$ | $T_\nu$ (K) | |
|---|---|---|
| | With ee | Without ee |
| 1 | 131 | 86 |
| 2 | 129 | 78 |
| 3 | 106 | 44 |
| 4 | 78 | 45 |
| 5 | 123 | 84 |
| 6 | 90 | 51 |
| 7 | 126 | 60 |
| 8 | 90 | 49 |
| 9 | 45 | 44 |
| 10 | 88 | 47 |

II D. Our results clearly demonstrate a hot-carrier regime, i.e., all electron temperatures $T_\nu$ are significantly higher than the lattice temperature $T_{\text{latt}}=44$ K. Moreover, one can notice that the electron temperature depends on the subband and, for example, is lower for level 6 than for level 1. Compared to the values obtained without electron–electron scattering, subband temperatures are higher, showing that carrier–carrier interaction warms up the distribution. Furthermore, one observes that subbands 1 and 2 have approximately the same subband temperature of about 130 K. Electron–electron scattering is partly responsible for the "mutual thermalization" which occurs between subbands close in energy ($\Delta\varepsilon_{12}=9$ meV), provided they strongly overlap and are significantly populated. This is due to so-called "biintrasubband" scattering processes $V_{\nu\mu\nu\mu}$, in the terminology of Harrison.[35] For these interactions, both principal and partner electrons remain in their initial subbands but exchange momentum and energy, redistributing the kinetic energy among the subbands.

This discussion demonstrates that the magnitude of the population inversion is very sensitive to electron–electron scattering through direct intersubband transitions. Moreover, carrier–carrier scattering strongly influences the distribution function and, therefore, details of electron dynamics.

## IV. CONCLUSION

We have proposed a method for modeling electron–electron scattering in Monte Carlo simulation of quantized systems that is efficient enough to be applied to many-subband systems such as QCL. The calculation of the very numerous form factors is tremendously speeded up by means of a Fourier decomposition procedure. Screening is treated beyond the single-subband approximation, using a model which, although quite simple, allows us to describe properly the behavior of both intra-and intersubband matrix elements of the Coulomb potential. The screening factors are calculated self-consistently during the simulation in order to account for the nonequilibrium nature of the distribution.

We have applied this model to a resonant phonon terahertz QCL. We have demonstrated that this QCL operates in a hot-carrier regime. Population inversion is strongly influenced by the screening model. We have confirmed the major role played by electron–electron scattering, which enhances population inversion at 3.4 THz, but on the contrary, limits the potential performance near 1 THz. In this regime, we have found a strong depopulation of the higher laser state through direct electron–electron transitions, suggesting that this nonradiative mechanism may strongly hinder the design of QCL at very long wavelengths.

## ACKNOWLEDGMENT

We are grateful to the Institut de Développement et des Ressources en Informatique Scientifique (IDRIS)–CNRS, France, for generous allocation of computer time.

[1] J. Faist, F. Capasso, D. L. Sivco, C. Sirtori, A. L. Hutchinson, and A. Y. Cho, Science **264**, 553 (1994).
[2] C. Gmachl, F. Capasso, D. L. Sivco, and A. Y. Cho, Rep. Prog. Phys. **64**, 1533 (2001).
[3] R. Köhler *et al.*, Nature (London) **417**, 156 (2002).
[4] M. Rochat, L. Ajili, H. Willenberg, J. Faist, H. Beere, G. Davies, E. Linfield, and D. Ritchie, Appl. Phys. Lett. **81**, 1381 (2002).
[5] B. S. Williams, H. Callebaut, S. Kumar, Q. Hu, and J. L. Reno, Appl. Phys. Lett. **82**, 1015 (2003).
[6] B. S. Williams, S. Kumar, H. Callebaut, Q. Hu, and J. L. Reno, Appl. Phys. Lett. **83**, 2124 (2003).
[7] C. Jacoboni and L. Reggiani, Rev. Mod. Phys. **55**, 645 (1983).
[8] R. C. Iotti and F. Rossi, Phys. Rev. Lett. **87**, 146603 (2001).
[9] M. A. Osman and D. K. Ferry, Phys. Rev. B **36**, 6018 (1987).
[10] S. M. Goodnick and P. Lugli, Phys. Rev. B **37**, 2578 (1988).
[11] A. Mošková and M. Moško, Phys. Rev. B **49**, 7443 (1994).
[12] M. Dür, S. M. Goodnick, and P. Lugli, Phys. Rev. B **54**, 17794 (1996).
[13] J. H. Smet, C. G. Fonstad, and Q. Hu, J. Appl. Phys. **79**, 9305 (1996).
[14] S.-C. Lee and I. Galbraith, Phys. Rev. B **59**, 15796 (1999).
[15] R. C. Iotti and F. Rossi, Semicond. Sci. Technol. **19**, S323 (2004).
[16] S.-C. Lee and A. Wacker, Appl. Phys. Lett. **83**, 2506 (2003).
[17] J.-L. Thobel, L. Baudry, P. Bourel, F. Dessenne, and M. Charef, J. Appl. Phys. **74**, 6274 (1993).
[18] D. J. BenDaniel and C. B. Duke, Phys. Rev. **152**, 683 (1966).
[19] J.-L. Thobel, O. Bonno, F. Dessenne, and H. Boutry, J. Appl. Phys. **92**, 5286 (2002).
[20] R. C. Iotti and F. Rossi, Appl. Phys. Lett. **78**, 2902 (2001).
[21] P. Borowik and J.-L. Thobel, J. Appl. Phys. **84**, 3706 (1998).
[22] D. Pines and D. Bohm, Phys. Rev. **85**, 338 (1952).
[23] M. Moško, A. Mošková, and V. Cambel, Phys. Rev. B **51**, 16860 (1995).
[24] M. Moško and A. Mošková, Phys. Rev. B **44**, 10794 (1991). Note that the scattering probability employed in the Monte Carlo simulation is computed using only one half of the rate in Eq. (3) to avoid double counting.
[25] J.-L. Thobel, L. Baudry, F. Dessenne, M. Charef, and R. Fauquembergue, J. Appl. Phys. **73**, 233 (1993).
[26] The computational cost of the evaluation of the Fourier coefficients is reduced using $\gamma_\sigma^{\nu'\nu}=(\gamma_{-\sigma}^{\nu\nu'})^*$.
[27] P. J. Price, Ann. Phys. (N.Y.) **133**, 217 (1981). The form factors are also used to compute other scattering rates, for example, scattering with polar optic or acoustical phonon involves overlap factors $F_{\nu\nu\mu\mu}(Q)$.
[28] M. V. Fischetti, J. Appl. Phys. **89**, 1232 (2001).
[29] S.-C. Lee and I. Galbraith, Phys. Rev. B **55**, R16025 (1997).
[30] Equations (15) are valid for the case of parabolic bands. Note that we multiply Eq. (15b) by an extra factor 2 in order to account for the symmetry of indices $(\xi,\xi')$ of Eq. (11).
[31] S. M. Goodnick and P. Lugli, Appl. Phys. Lett. **51**, 584 (1987).
[32] S. M. Goodnick and P. Lugli, Phys. Rev. B **38**, 10135 (1988).
[33] M. Moško, V. Cambel, and A. Mošková, Phys. Rev. B **46**, 5012 (1992).
[34] H. Callebaut, S. Kumar, B. S. Williams, Q. Hu, and J. L. Reno, Appl. Phys. Lett. **83**, 207 (2003).
[35] P. Harrison, Appl. Phys. Lett. **75**, 2800 (1999).